CHALMERS
UNIVERSITY OF TECHNOLOGY

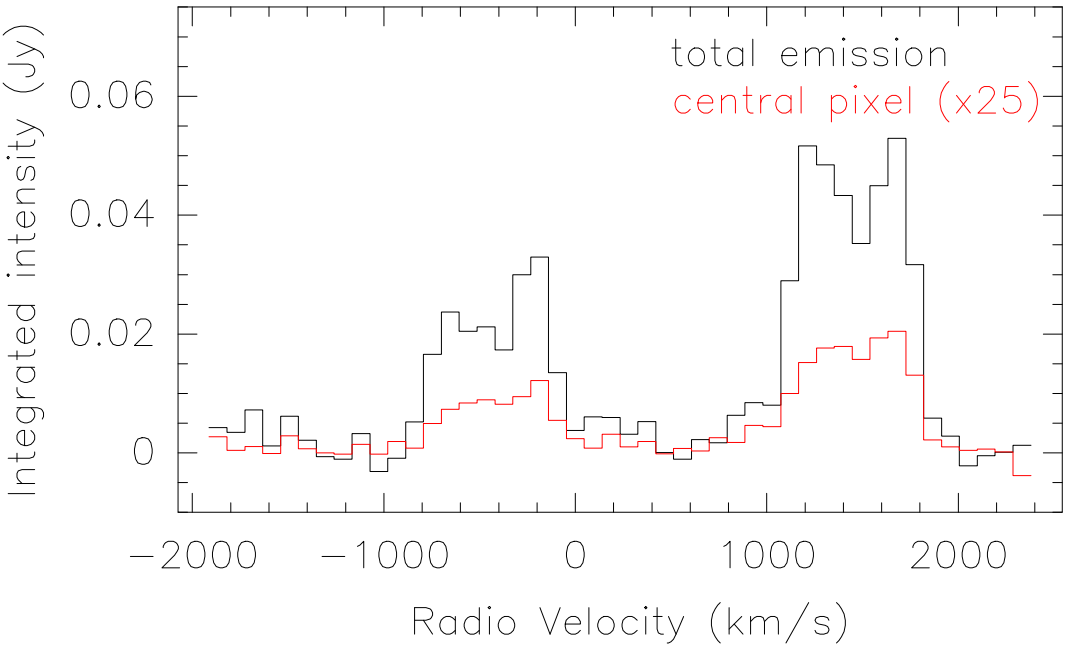

Vibrationally excited HCN and outflows in (Ultra-) Luminous Infrared Galaxies

Master's thesis in Physics and Astronomy

FILIPPA HALLQVIST

Department of Earth and Space Sciences
CHALMERS UNIVERSITY OF TECHNOLOGY
Gothenburg, Sweden 2017

Master's thesis 2017

Vibrationally excited HCN and outflows in (Ultra-) Luminous Infrared Galaxies

FILIPPA HALLQVIST

CHALMERS
UNIVERSITY OF TECHNOLOGY

Department of Earth and Space Sciences
Radio Astronomy and Astrophysics, Extragalactic Astrophysics
Chalmers University of Technology
Gothenburg, Sweden 2017

Vibrationally excited HCN and outflows in (Ultra-) Luminous Infrared Galaxies
Filippa Hallqvist, filippahallqvist@gmail.com

Supervisor: Susanne Aalto, Francesco Costagliola and Sabine König,
Earth and Space Sciences

Department of Earth and Space Sciences
Group: Radio Astronomy and Astrophysics, Extragalactic Astrophysics
Chalmers University of Technology
SE-412 96 Gothenburg
Telephone +46 31 772 1000

Onsala Space Observatory
SE-439 92 Onsala, Sweden
+46 31-772 5500

Cover: Spectrum showing detections of HCO^+ J=3-2, HCN-VIB J=3-2 and HCN J=3-2 in UGC 5101. The central channel at a velocity of 0 km s^{-1} is centered at the redshifted frequency 257.071 GHz. Figure from Hallqvist et al. (in prep.).

Typeset in LaTeX
Gothenburg, Sweden 2017

Vibrationally excited HCN and outflows in (Ultra-) Luminous Infrared Galaxies
FILIPPA HALLQVIST
Department of Earth and Space Sciences
Chalmers University of Technology

Abstract

To understand what happens in galaxy nuclei and how central super-massive black holes (SMBHs) evolve and affect their surroundings is made very difficult by large masses of obscuring gas and dust, complicating observations at optical and infrared wavelengths. Instead, it has been suggest that HCN in its first vibrational state (HCN-VIB) is an excellent tracer of these deeply buried nuclei, making it possible to observe dynamics and temperatures of regions that would remain hidden at shorter wavelengths. The existence of HCN-VIB may also trace a period of rapid growth of the central SMBH, just before the onset of fast galactic outflows. However, the samples used to suggest this trend have so far been very small and any correlation would need to be statistically determined.

The aim of this thesis is to explore if a correlation exists between the ratio of HCN-VIB line luminosity and the far infrared luminosity (L(HCN-VIB)/L_{FIR}), and molecular outflows or inflows in (Ultra) Luminous Infrared Galaxies ((U)LIRGs). This is done by collecting observational data of the HCN-VIB line from the literature and comparing it to outflow and inflow velocities traced by OH absorption. To establish if a correlation exists, Fisher's exact test is performed. As a case study, the vibrational temperature and mass is also estimated for the LIRG UGC 5101.

We find that UGC 5101 has a vibrational temperature of $T_{vib} = 442$ K while the dynamical mass is estimated to $M_{dyn}(r < 378 \text{ pc}) = 5.6 \times 10^{10}\ M_\odot$. The dense gas mass is estimated to $M_{dense} = 9.5 \times 10^{8}\ M_\odot$. Finally, performing Fisher's exact test on the sample of galaxies, a likely correlation between high L(HCN-VIB)/L_{FIR} ratios and a lack of fast outflows is found.

Keywords: Galaxies, Vibrational HCN, UGC 5101, Outflows.

Acknowledgements

First of all I would like to thank my supervisors Susanne Aalto, Sabine König and Francesco Costagliola for all the help, motivation and inspiring conversations. I would also like to thank my opponent Negar Entekhabi for valuable input on my thesis. Additionally I would like to thank the department of Earth and Space Sciences and Onsala Space Observatory for providing me with a place to sit and work as well as arranging interesting seminars. More importantly I would like to thank all the people associated for your welcoming attitudes, interesting discussions, lunch walks and company. You have made my time the best possible!

Finally I'd like to thank my family and friends for all the support and for having the energy to listen to me going on and on about my thesis. I especially want to thank Olle Elias for both helping me with discussions about statistical tests, as well as all the patience, love and support throughout this sometimes stressful period.

Filippa Hallqvist, Gothenburg, April 2017.

Contents

List of Figures x

List of Tables xii

Nomenclature xv

1 Introduction 1

2 Theory 3
2.1 Introduction to measures of temperature . . . 4
2.2 Spectral lines and molecular spectroscopy . . . 4
2.2.1 Rotational and Vibrational Spectra . . . 5
2.2.1.1 The rotational-vibrational spectrum of HCN . . . 6
2.2.2 HCN as a tracer of dense gas . . . 7
2.2.2.1 Methods of excitation . . . 8
2.3 Galaxies and galaxy nuclei . . . 9
2.3.1 Active Galactic Nuclei . . . 9
2.3.2 Starburst . . . 11
2.3.3 Obscured Nuclei . . . 12
2.3.4 (Ultra-)Luminous Infrared Galaxies . . . 12
2.3.5 Galactic outflows and winds: Feedback . . . 12
2.4 Galactic property estimation . . . 13
2.4.1 Calculation of rotational and vibrational temperatures . . . 13
2.4.2 Calculation of the dynamical mass and the dense gas mass . . . 14
2.5 Fisher's exact test . . . 15

3 Method 17
3.1 Vibrational HCN and outflow data . . . 17
3.2 Sample . . . 17
3.3 Calculation of line luminosities . . . 17
3.4 UGC 5101 . . . 18
3.4.1 The vibrational temperature . . . 19
3.4.2 The dynamical mass and dense gas mass . . . 19
3.5 Statistical tests . . . 20

4 Results 21
4.1 UGC 5101 . . . 21

4.1.1 The vibrational temperature 21
4.1.2 The rotational velocity 21
4.1.3 Dynamical and dense gas masses 22
4.2 Vibrational HCN and outflows in (U)LIRG:s 23
4.3 Statistical tests 23
4.3.1 L(HCN-VIB)/L_{FIR} vs OH outflows 23
4.3.2 L(HCN-VIB)/L_{FIR} vs outflows with additional CO data 23
4.3.2.1 R=1×10^{-8} considered a high ratio 25
4.3.2.2 R=1×10^{-8} considered a low ratio 26

5 Discussion **27**
5.1 UGC 5101 27
5.2 HCN-VIB and Outflows 28
5.2.1 The contradicting sources 29
5.3 Limitations on the data 30
5.4 The statistical analysis 31

6 Conclusion and Outlook **33**

Bibliography **35**

List of Figures

2.1 The black body spectrum for three different temperatures. 3

2.2 Energy diagram for rotational levels J of HCN in $v = 0$ and $v = 1$. For $v = 1$ the degenerate states e and f is shown. The energy values are from from the Cologne Database for Molecule Spectroscopy (CDMS) and given in Kelvin. The figure is created by Aalto et al. (2015a). . . 6

2.3 Diagram showing the different vibrational modes for a linear triatomic molecule. The arrows represent the starting motion of the atoms. . . 7

2.4 Spectrum showing HCO^+ J=3-2, HCN J=3-2 $v_2 = 1f$ and HCN J=3-2 peaks. Here the HCO^+ J=3-2 line lies close to the HCN-VIB, making them blend with each other. Note that the x-axis is given in radio velocity. This relate to the frequency by $\nu_{\mathsf{obs}} = \nu_{\mathsf{rest}}(1 - \mathrm{v}_{\mathsf{radio}}/c)$. Figure adapted from Hallqvist et al. (in prep.). 8

2.5 Figure showing the inner structure of a galaxy with an active nucleus. Credit: Claudio Ricci - `http://www.isdc.unige.ch/~ricci/Website/Active_Galactic_Nuclei.html` 10

2.6 Diagram illustrating how the angle of an AGN with a jet will make the same type of source appear differently when observed. Figure by Ron Kollgaard for Wikimedia Commons, `https://commons.wikimedia.org/w/index.php?curid=6654413`. 11

3.1 Hubble space telescope image of UGC 5101. Credit: NASA, ESA, the Hubble Heritage (STScI/AURA)-ESA/Hubble Collaboration and A. Evans 19

4.1 Position velocity diagram of HCN in UGC 5101. The contours mark signals in steps of intensities of 3σ. The x axis gives the position in arcseconds while the y axis give the velocity in km s^{-1}. Figure from Hallqvist et al. (in prep.). 22

4.2 Scatter plot with L(HCN-VIB)/$\mathrm{L}_{\mathsf{FIR}}$ on the x-axis and OH v_{50}(abs) velocities from Veilleux et al. (2013) on the y-axis. Sources with both HCN J=3-2 and J=4-3 detections have only been counted once and is marked by circles or squares respectively, upper limits are shown as arrows. Galaxies classified as ULIRGS are given blue markers while LIRGs are given red. 25

4.3 Scatter plot with L(HCN-VIB)/L_{FIR} on the x-axis and OH v_{84}(abs) velocities from Veilleux et al. (2013) on the y-axis. Sources with both HCN J=3-2 and J=4-3 detections have only been counted once and is marked by circles or squares respectively, upper limits are shown as arrows. Galaxies classified as ULIRGS are given blue markers while LIRGs are given red. 26

5.1 Scatter plot with L(HCN-VIB)/L_{FIR} on the x-axis and equivalent width W_{eq} from González-Alfonso et al. (2015) on the y-axis. Note the log-scale on the y-axis. Arrows indicate upper limits and sources placed on the y-axis are non-detections. 29

5.2 Scatter plot with L(HCN-VIB)/L_{FIR} on the x-axis and OH velocities from Veilleux et al. (2013) on the y-axis. Sources with both HCN J=3-2 and J=4-3 detections have only been counted once and is marked by circles or squares respectively, arrows represent upper limits. Galaxies classified as ULIRGS are given blue markers while LIRGs are given red. 31

List of Tables

2.1 HCN molecular line properties 9
2.2 A typical Fisher-matrix. The categories are chosen so that category 1 and 2 can not contain the same sources, the same is valid for categories 3 and 4. 15

3.1 Sample galaxies 18

4.1 Observed properties for UGC 5101 21
4.2 Estimated properties for UGC 5101 22
4.3 L(HCN-VIB) vs. L_{FIR} 24
4.4 Fisher-matrix for the 12 sources with known OH velocities. 25
4.5 Fisher-matrix for 17 sources with OH , CO and H_2 outflow data included. R=1×10^{-8} is considered a strong ratio. 25
4.6 Fisher-matrix for 17 sources with OH , CO and H_2 outflow data included. R=1×10^{-8} is considered a weak ratio. 26

5.1 Fisher-matrix for the 12 sources with known OH velocities, assuming 15250+3609 has a HCN-VIB detection. 30

Nomenclature

Units

	Arcsecond, $1'' = \frac{1}{3600}^\circ$
Jy	Jansky, an astronomical unit of spectral energy, $1\,\mathrm{Jy} = 10^{-26}\,\mathrm{W/(m^2\,Hz)}$
L	Solar luminosity, an astronomic measure corresponding to the sun's mean luminosity $1\,\mathrm{L}_\odot = 3.827 \cdot 10^{26}\,\mathrm{W}$
M	Solar mass, an astronomical measure corresponding to the sun's mass $1\,\mathrm{M}_\odot = 1.989 \cdot 10^{30}\,\mathrm{kg}$
pc	Parsec, $1\,\mathrm{pc} = 3.086 \cdot 10^{16}\,\mathrm{m}$

Physical Quantities

λ, ν	Wavelength and frequency, for photons related by $\nu = \dfrac{c}{\lambda}$
τ	The optical depth, a measure of the transparency of a medium to a certain wavelength of light.
D_L	Luminosity distance, the distance defined by the relation between flux and luminosity integrated over all frequencies: $D_\mathrm{L} = \sqrt{L/(4\pi S)}$.
S_ν	Spectral flux, a measure of the radiated intensity at a specific frequency commonly given in Jy
z	Redshift, defined as $1 + z = \frac{\nu_\mathrm{rest}}{\nu_\mathrm{obs}}$
N	Column density, a 2-dimensional density measured along the line of sight.

Constants

c	The speed of light in a vacuum, $c = 2.998 \cdot 10^8\,\mathrm{m\,s^{-1}}$
G	The gravitational constant, $G = 6.67 \cdot 10^{-11}\,\mathrm{m^3\,kg^{-1}\,s^{-2}}$
h	Planck's constant, $h = 6.626 \cdot 10^{-34}\,\mathrm{Js}$
k	Boltzmann's constant, $k_B = 1.381 \cdot 10^{-23}\,\mathrm{J\,K^{-1}}$

Abbreviations

(U)LIRG	(Ultra) Luminous Infrared Galaxy
AGN	Active Galactic Nuclei
ALMA	Atacama Large Millimeter/Submillimeter Array
CDMS	Cologne Database of Molecular Spectroscopy
FIR	Far-infrared
FWHM	Full Width at Half Maximum
HCN-VIB	Vibrationally exited HCN
IR	Infrared
ISM	The interstellar medium
NED	NASA/IPAC Extragalactic Database
QSO	Quasi-stellar object
SFR	Star Formation Rate

SMBH Super Massive Black Hole

Wavelength regimes

FIR long-wave infrared light with wavelengths between 15 μm – 1 mm.

IR Light with wavelengths between 700 nm – 1 mm. Sometimes also called heat radiation.

Optical Wavelengths observable by the human eye, typically around 350 – 700 nm

Radio Wavelengths longer than 1 mm

Submillimeter Wavelengths somewhat shorter than 1 mm

UV Wavelengths between 100 – 350 nm

1
Introduction

It is possible to explore a range of phenomena in space by observing at different wavelengths of the electromagnetic spectrum. In fact, humanity has observed stars at optical wavelengths since we first saw the night sky, but only during the last century discovered how to observe at other parts of the spectrum. With these discoveries it became possible to observe gas and dust not just as something that obscured starlight, but as emitting matter. A lot has been learned about gas and dust by observing at sub-mm wavelengths or in the infrared. It is at these wavelengths we enter the world of molecular transitions and get tools to observe the interstellar medium (ISM) in it self. The majority of the ISM is made up by hydrogen, but also more complex molecules form and exist in the ISM. These provide valuable information about their surrounding medium through line emission from rotational and vibrational transitions.

Some of the regions where we can learn a lot by observing rotational or vibrational transitions are the central parts of galaxies with active galactic nuclei (AGN). These galaxies are gas-rich and harbour one or several growing super massive black holes (SMBHs) that make the central parts of the galaxy glow much stronger than the rest of the galaxy. The gas and dust in the center of these galaxies can be so dense that it blocks out emission from the innermost parts, making it difficult or even impossible to see what is going on. Still, these regions are extremely interesting to study in order to understand how SMBHs evolve, and how this in turn is connected to the evolution of the host galaxy.

One way that the SMBH affect the host galaxy is through outflows (Sect. 2.3.5). These are launched from very close to the SMBH and carry gas and dust outward in the galaxy, redistributing the ISM. At the same time, the gravitational pull from the SMBH may lead to inflows of gas that has left, or never has had, a stable orbit.

By using molecular spectroscopy and the knowledge of how certain molecules behave at different temperatures and densities, it is possible to see into regions that are obscured when observing at shorter wavelengths. Intrinsic properties of the molecules and atoms in the gas make the medium more transparent to photons with longer wavelengths. During the last decades, molecules like CO, OH and HCN have been used to trace dynamics, masses and temperatures of gas (Draine, 2010). Today these molecules, together with a few more, make up a tool box with tools available depending on what parts or properties the observer is interested in.

Aalto et al. (2015) find that vibrationally excited emission of the HCN molecule, from here on written as HCN-VIB, is an excellent tracer of deeply obscured galaxy nuclei. Since HCN-VIB requires high densities to exist, as well as a temperature over 100 K, it can thrive in the nucleus of a galaxy. In the same article it was suggested

that HCN-VIB emission might be connected to a lack of fast outflows, indicative of the SMBH being in a phase of rapid growth. However this suggestion was based on a very small sample and is in need of being statistically determined. This problem is what will be attempted to solve in this thesis.

In order to compare the strength of HCN-VIB emission between galaxies a ratio needs to be chosen. Otherwise the strength would naturally follow galaxy properties like size and distance making it incomparable. By choosing to divide the line luminosity (L(HCN-VIB)) with the far infrared luminosity (L_{FIR}) of the galaxy, it becomes possible to compare the results between galaxies.

The far-infrared luminosity is a continuum luminosity which tells us about the heat radiation from dust and cool gas with temperatures around 50-200 K. Regions with dense gas often radiate strongly in the far infrared, but the high density is also a prerequisite for detecting HCN-VIB. The amount of HCN-VIB emission in the same region as the far infrared emission, as well as the the temperature of the exciting dust source is something that will affect the ratio (Aalto et al., 2015b).

The research question central to this thesis is if there exists a correlation between the strength of the L(HCN-VIB)/L_{FIR} ratio and the existence of molecular outflows or inflows. The aim is to answer this question by extending the original sample presented in Aalto et al. (2015b) with sources from the Veilleux et al. (2013) sample that have reported HCN-VIB observations. A case study of the galaxy UGC 5101 has also been made based on not yet published data from Hallqvist et al. (in prep.), adding to our sample of galaxies with HCN-VIB observations.

The rest of this work will be structured with an overview of the theoretical framework presented in Chapter 2. This includes a background to galactic nuclei, molecular spectroscopy and Fisher's exact test. The sample of galaxies together with motivations and adaptations of the estimation methods are presented in Chapter 3, as well as further explanations of the statistical analysis. The results are then presented in Chapter 4 while a discussion of the result is found in Chapter 5. Finally the conclusions are presented in Chapter 6.

2

Theory

One of the most fundamental equations in astrophysics is Planck's law, which describes the spectral distribution for electromagnetic radiation in thermodynamic equilibrium. The spectral flux S_ν is related to the frequency ν and temperature T by

$$S_\nu = \frac{2h\nu^3}{c^2} \frac{1}{e^{\frac{h\nu}{kT}} - 1}. \tag{2.1}$$

This is also more commonly known as *black body radiation*, and can be used to approximate both the radiation from stars and from gas. Fig. 2.1 show the black body spectra for three different temperatures.

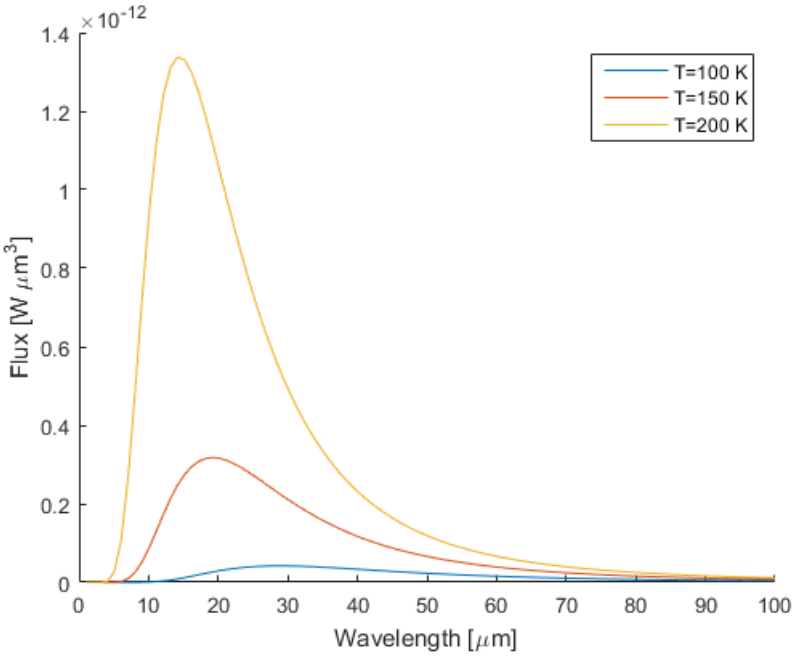

Figure 2.1: The black body spectrum for three different temperatures.

At long wavelengths, or more correctly when $h\nu \quad kT$, Planck's law can approximated by what is known as the Rayleigh-Jeans law:

$$S_\nu = \frac{2\nu^2 k}{c^2} T. \tag{2.2}$$

This is a linear relation between the flux and the temperature, making it possible to describe signals in terms of temperatures.

2.1 Introduction to measures of temperature

In radio astronomy, temperature is commonly used to describe the strength of signals. Here follows a short summary with explanations of the different measures of temperature used in this work.

- Brightness temperature, $\mathrm{T_B}$: The brightness temperature is the temperature corresponding to the measured flux, S_ν, using the Rayleigh-Jeans law.

$$T_B = \frac{c^2}{2\nu^2 k} S_\nu \tag{2.3}$$

  Note that Rayleigh-Jeans law is an approximation of Planck's law in the limit $h\nu \quad kT_B$. It is only when this condition is fulfilled that T_B has a physical meaning, otherwise it is just a way to describe the strength of the signal.
- Kinetic temperature, T_K:

$$T_K = \frac{1}{3k} m\mathrm{v}^2. \tag{2.4}$$

  This temperature correspond to the heat from the motion of a particle with mass m and velocity v.
- Excitation temperature, $\mathrm{T_{ex}}$:

$$T_{\mathsf{ex}} = \frac{E_{ul}/k}{\ln \frac{g_u n_l}{g_l n_u}} \tag{2.5}$$

  This is the temperature needed to excite emission of a certain transition and describes the occupation of the energy levels of a molecule using a Boltzmann distribution. Here n_u and n_l are the number densities of the upper and lower state, g_u and g_l their respective statistical weights and E_{ul} the energy difference between the levels.
  T_{ex} can also be called T_{vib} or T_{rot} depending on if it describes vibrational or rotational transitions.

The brightness temperature is related to the excitation temperature by

$$\mathrm{T_B} = \mathrm{T_{ex}}(1 - \mathrm{e}^{-\tau}), \tag{2.6}$$

where τ is known as the *optical depth* of the transition. The optical depth describes how far radiation of a certain wavelength can penetrate the surrounding medium. If the observed system is in local thermodynamic equilibrium (LTE), $\mathrm{T_{ex}}$=$\mathrm{T_K}$. For a more in depth description of temperatures, please consult Wilson, Rohlfs & Hüttemeister (2009).

2.2 Spectral lines and molecular spectroscopy

A spectral line is usually described by one frequency, but in reality the line is not infinitely thin. There are primarily three types of line broadening, where the most fundamental is the *natural broadening*. This type is closely related to Heisenberg's principle of uncertainty, since an uncertainty in the energy of states in the transition

exists. This uncertainty connects to the finite life time of an excited state and leads to broader lines if the lifetime is short and less broadening if the lifetime is long.

Another type of broadening is *Doppler broadening*, which arises due to thermal motion of particles. Since some of the emitting molecules will be moving away and other towards us, the transition lines will be Doppler shifted, and create a broadening of the observed line. If the velocity distribution is Maxwellian, as assumed in the case of local thermal equilibrium, the 1D projected velocity distribution will be Gaussian. When observing molecular lines it is therefore common to make Gaussian fits of the observed peaks (Sindhu, 2012).

A third way of broadening is *collisional broadening*. If the molecules undergo collisions there is a probability that a molecule in an excited state might undergo a radiationless transition to a lower state. This reduces the lifetime of a state thus leading to broader lines (Sindhu, 2012).

The width of a spectral line can therefore tell us about the physics in the area where the emission arises. There are several ways of characterising the width, but one of the most common ways is simply called *line width* and is given in frequency or velocity. The line width, Δv, is usually taken as the full width at half maximum (FWHM) and will for a Gaussian curve relate to the dispersion as $\sigma = \mathrm{FWHM}/2\sqrt{2\ln 2}$.

2.2.1 Rotational and Vibrational Spectra

After atoms have formed a molecule, the new shape and symmetry of the system makes it possible for it to rotate or vibrate. If the molecule has a permanent dipole moment these new degrees of freedom give rise to a spectrum, dependent on the properties of the molecule in question (Sindhu, 2012). Rotational and vibrational spectra can be found around microwave and infrared frequencies.

The simplest case to describe where rotational and vibrational excitation occur is the diatomic molecule. The rotational spectrum may in this case be approximated by the rigid rotor approximation, assuming a fixed distance between the atoms during the rotation. Using this assumption the moment of inertia for the molecule is given by $I = \mu r^2$, where the reduced mass is given by

$$\mu = \frac{m_A m_B}{m_A + m_B}, \tag{2.7}$$

and r is the distance between the center of the atoms. By solving the Schrödinger equation for a rigid rotator we get

$$\frac{E}{hc} = \frac{h}{8\pi^2 cI} J(J+1) = BJ(J+1), \tag{2.8}$$

where $B = \frac{h}{8\pi^2 cI}$ and J is called the rotational quantum number. Rotational transitions are only possible when ΔJ= $\pm$1 and are usually written on the form J=l_i-l_f. Here l_i refers to the initial rotational energy level for the transition, and l_f to the final. E.g J=2-1 describe the emission line created when a molecule goes from the second to the first rotational state. To express absorption it is the other way around,

J=1-2. Together, these rotational states make up what is called a rotational ladder, where each transition between levels can be seen as line emission or absorption (Sindhu, 2012).

Vibrational transitions in molecules may be described by regarding the atoms as mass points connected by an elastic spring. Hence the vibrational frequency of the molecule is given by $\nu = \frac{1}{2\pi}\sqrt{\frac{k}{\mu}}$, where k is the force constant of the bond. This kind of conservative system may be approximated as a harmonic oscillator, with its solution to the Schrödinger equation being

$$E = h\nu(v + \frac{1}{2}). \tag{2.9}$$

Here v is the vibrational level of the molecule while the extra term of $1/2$ is due to the "zero-point" energy which emerges since the quantum vibrator can not exist at the minimum potential. Hence a pure vibrational transition $v - (v - 1)$ would have the energy $h\nu$.

Together, the vibrational and rotational transitions form the "rotational-vibrational spectrum" of a molecule.

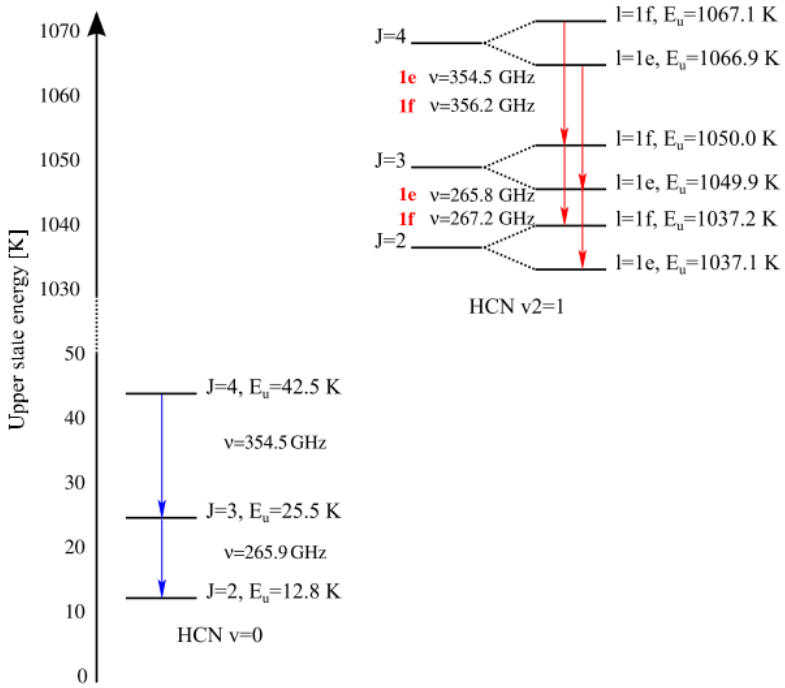

Figure 2.2: Energy diagram for rotational levels J of HCN in $v = 0$ and $v = 1$. For $v = 1$ the degenerate states e and f is shown. The energy values are from from the Cologne Database for Molecule Spectroscopy (CDMS) and given in Kelvin. The figure is created by Aalto et al. (2015a).

2.2.1.1 The rotational-vibrational spectrum of HCN

The HCN molecule is triatomic and more complex than the diatomic molecules. Instead of just one vibrational mode, triatomic molecules have three modes (asym-

metrical, bending and symmetrical) and some of these may be degenerate (Wilson, Rohlfs & Hüttemeister, 2009). A diagram of how the atoms move in the different vibrational modes is shown in Fig. 2.3. Fortunately, experimental determinations

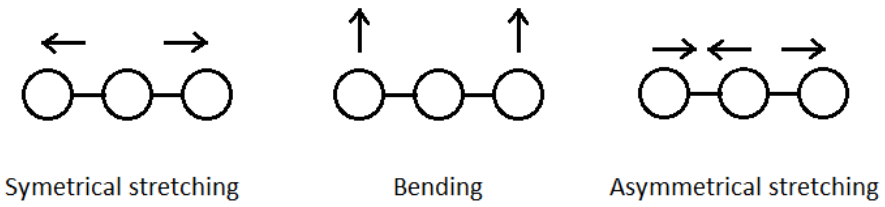

Figure 2.3: Diagram showing the different vibrational modes for a linear triatomic molecule. The arrows represent the starting motion of the atoms.

of the different vibrational modes and frequencies have been made. For the HCN molecule the simplest of the modes is the v_2 bending mode, since it has the lowest energies. This mode is degenerate and the different degenerate states are called $l = 1e$ and $l = 1f$ where $1f$ has the slightly higher energy. An energy diagram for HCN and its rotational and vibrational states can be found in Figure 2.2. Note that the energy levels are expressed as temperature given in Kelvin using the relation $E = kT$. Since the frequency of especially the HCN J=3-2 $v_2 = 1e$ and HCN J=4-3 $v_2 = 1e$ lines are very close to that of the often stronger HCO^+ J=3-2 and J=4-3 lines, it will be impossible to tell them apart in extra-galactic sources. Instead the more energetic of the degenerate vibrational transitions, $v_2 = 1f$ can be used. This will increase the chance of being able to discern the transition from HCO^+, depending on the observed line widths. An exampel of a spectrum where HCN-VIB is detected can be seen in Fig. 2.4. Properties of HCN J=3-2 $v_2 = 1f$ and HCN J=4-3 $v_2 = 1f$ can be found in Table 2.1.

2.2.2 HCN as a tracer of dense gas

An overwhelming majority of the dense gas in the universe consists of molecular hydrogen, H_2, which in it self is very hard to observe since it lacks a permanent dipole moment at mm wavelengths. Since H_2 is the most abundant molecule in the universe, astronomers need to observe so called tracers to be able to infer properties of the H_2 gas. These tracers are usually asymmetrical molecules with permanent dipole moments, making them possible to observe by rotational or vibrational transitions (see Sect. 2.2.1). Even though these molecules are far less abundant than H_2, the total number in gas rich environments will be enough for detection. Commonly used tracers include molecules like CO, HCN and HCO^+. In fact, different molecules trace different aspects of the gas, and the choice of molecule affects what regions will be observable.

HCN is appropriate for observations of dense gas regions, mainly due to its high critical density (see Sect. 2.2.2.1) and energy levels in its rotational and vibrational ladder (See Table 2.1). These energy levels may be excited by continuous infrared radiation from warm gas. Gao & Solomon (2004a) suggest a relation between the HCN

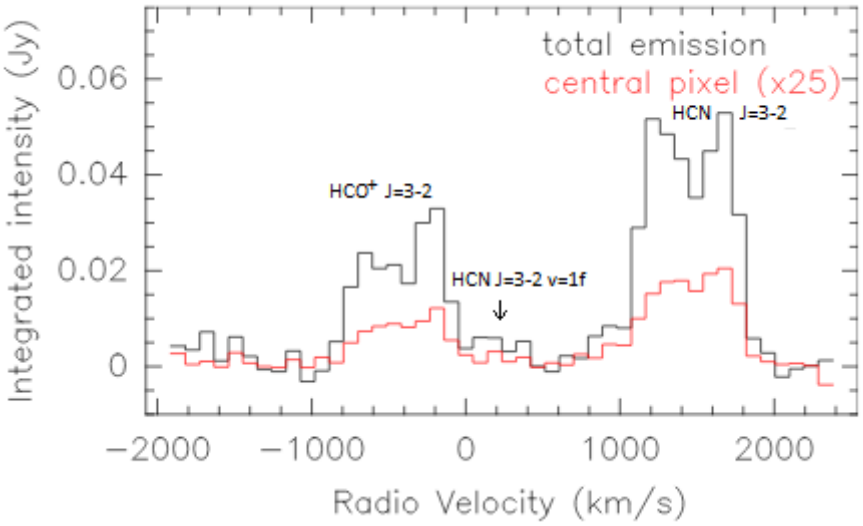

Figure 2.4: Spectrum showing HCO^+ J=3-2, HCN J=3-2 $v_2 = 1f$ and HCN J=3-2 peaks. Here the HCO^+ J=3-2 line lies close to the HCN-VIB, making them blend with each other. Note that the x-axis is given in radio velocity. This relate to the frequency by $\nu_{obs} = \nu_{rest}(1 - v_{radio}/c)$. Figure adapted from Hallqvist et al. (in prep.).

luminosity and dense gas mass and also find a linear correlation between the HCN J=1-0 transition and the star formation rate (SFR), indicating that HCN traces dense gas involved in star formation (Gao & Solomon, 2004b). Other commonly used HCN transition are the J=3-2 and J=4-3 rotational transitions.

2.2.2.1 Methods of excitation

There are two major ways to excite a molecule in its rotational-vibrational ladder and that is by collision or radiation. Collisional excitation transforms the energy from a collision into internal energy in the molecule, while radiative excitation is driven by photons of energies corresponding to a certain transition.

For a molecule to be radiatively excited, it needs to be excited by photons of the same energy as the energy gap between the vibrational levels. This wavelength can be calculated using the relation

$$\lambda = \frac{hc}{E_{ul}}, \tag{2.10}$$

where h is the Planck constant, c is the speed of light and E_{ul} the energy between the states. This energy is often given in terms of temperature, using that $E_{ul} = kT$. For HCN (Table 2.1), the difference between the first vibrational state and the ground state is approximately 1024 K. This roughly correspond to a wavelength of 14 μm, which is in the infrared part of the spectrum.

To know if a molecule is radiatively or collisionaly excited, the gas density may be compared with the *critical density*. This density is the density when collisional

Table 2.1: HCN molecular line properties

Line	Frequency (GHz)	E_u/k (K)
(1)	(2)	(3)
HCN $J = 3 - 2$	265.89	25.5
HCN $J = 3 - 2$ $v_2 = 1f$	267.20	1050.0
HCN $J = 4 - 3$	354.51	42.5
HCN $J = 4 - 3$ $v_2 = 1f$	356.26	1067.1

Note: Col. (1): Transition line. Col. (2): Rest-frame frequency. Col. (3): Upper energy level. Values in Col. (2) and (3) are from the Cologne Database of Molecular Spectroscopy (CDMS) (Müller et al. 2005) via Splatalogue (http://www.splatalogue.net).

excitations balances radiative excitation:

$$n_{\mathsf{crit}} \approx \frac{A_{ul}}{\sigma v}. \tag{2.11}$$

Here A_{ul} is the Einstein rate coefficient for the excitation and σv is notation for the collisional rate coefficient for the molecule. For densities higher than the critical density the excitations will be dominated by collisions, while lower densities are dominated by radiative processes. For vibrationally excited HCN, this critical density exceeds 10^{10} cm^{-3} (Ziurys & Turner, 1986).

Carroll & Goldsmith (1981) describe how infrared pumping can occur when the infrared rate is faster than the rotational decay rate. Higher and higher states will be populated until an equilibrium is reached. This way a population may be found in a higher rotational-vibrational state than expected from the collisional excitation rate, since it has been "pumped" by the infrared radiation. For HCN this requires a $T_{\mathsf{vib}}(14\mu\mathrm{m}) \geq 100$ K (Sakamoto et al., 2010).

2.3 Galaxies and galaxy nuclei

In this section a background to the type of galaxies treated in this work will be given. The focus lies on galactic nuclei and properties in the center of galaxies, and how these may be used to classify the whole galaxy.

2.3.1 Active Galactic Nuclei

In the center of galaxies there is one or multiple supermassive black holes (SMBHs) with masses ranging from 10^6 to $10^{10}\,M_\odot$. These SMBHs feed on the surrounding gas and dust in the galaxy and affect the evolution of their host galaxy both by feedback, such as jets and outflows (see Sect. 2.3.5), as well as by dynamical and gravitational effects. If there is plenty of material accreting onto the black hole the gas will heat up and radiate strongly in the X-ray spectrum, making the galaxy

nucleus extremely luminous. This nucleus is called an Active Galactic Nuclus (AGN) (Beckmann & Shrader, 2013).

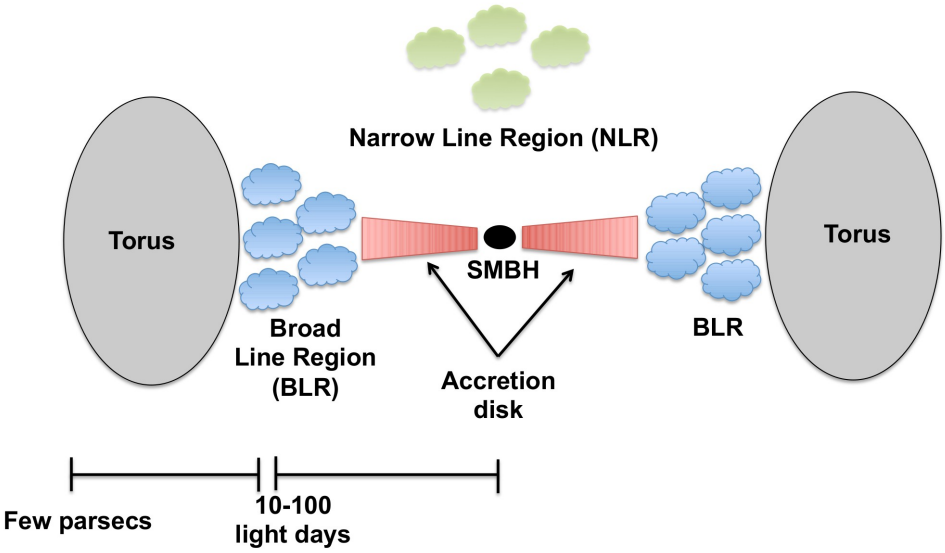

Figure 2.5: Figure showing the inner structure of a galaxy with an active nucleus. Credit: Claudio Ricci - `http://www.isdc.unige.ch/~ricci/Website/Active_Galactic_Nuclei.html`

An AGN typically consists of the central SMBH, an accretion disc and a surrounding torus of gas. Other components are the broad- and narrow line regions. The Broad line region (BLR) is a small region consisting of cooler gas with high velocities, leading to the broad width of optical spectral lines. The narrow line region (NLR) is more distant and spatially extended, and contains cool but slower gas leading to the more narrow line widths. Both the the BLR and NLR can be seen in Fig.2.5, showing an illustration of the inner structure of an AGN.

Several classifications of AGNs exist depending on how strongly they radiate at different wavelengths and if the spectral lines appear broad or narrow. Some of them are: Seyfert galaxies, Radio galaxies, Quasars and Quasi stellar objects (QSOs). Quasar and QSO is sometimes used to describe the same type of object (Choudhuri, 2010). Seyfert galaxies are radio-quiet spiral galaxies with either broad or narrow emission lines divided into the subtypes Seyfert 1 and Seyfert 2 respectively. Radio galaxies are elliptical galaxies with active nuclei that emit strongly in the radio regime. Quasars are the strongest of the active galaxies and have an extremely compact radio source as well as broad emission lines. In comparison, QSO was originally used to describe radio-quiet objects.

In later years, a unification scheme for AGNs has been suggested, proposing that many of the objects are in fact of the same type, but seen from different viewing angles (e.g Antonucci, 1993; Urry & Padovani, 1995; Tran, 2003). The difference between a Seyfert 1 and a Seyfert 2 galaxy would be that the type 1 is observed face-on, meaning from the front, and type 2 seen edge-on, meaning from the side (Fig. 2.6). Edge-on, gas and dust in the torus would obscure the broad line region, while

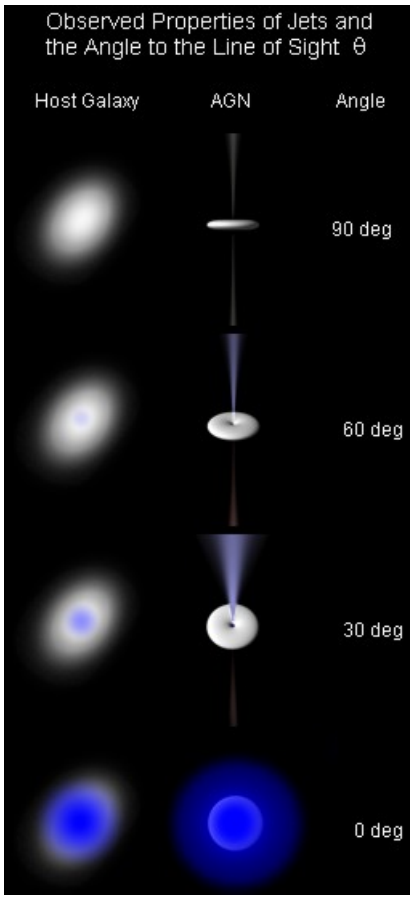

Figure 2.6: Diagram illustrating how the angle of an AGN with a jet will make the same type of source appear differently when observed. Figure by Ron Kollgaard for Wikimedia Commons, `https://commons.wikimedia.org/w/index.php?curid=6654413`.

the line of sight for a type 1 would be undisturbed making it possible to observe the broad lines.

2.3.2 Starburst

A starburst galaxy is a galaxy containing a region of extreme star formation, leading to a higher star formation rate (SFR) than the average galaxy. Star formation rates in starbursts usually range between 10-100 $M\ /yr$ on galactic scales, e.g the nearby Starburst galaxy M82 has a SFR of 10 $M\ /yr$. For comparison, the average SFR is 1.2 $M\ /yr$ in the Milky way (Lee, Murray & Rahman, 2012). Massive starformation is often triggered by galaxy mergers, which is when galaxies collide to create a new galaxy, or by close encounters between galaxies. Starburst galaxies are often recognized by their high SFRs, the high amount of gas available for star formation, and how fast this gas is being depleted. For a galaxy to be considered a starburst galaxy, it has to have a SFR higher than the previous average during its own history. A region within a galaxy may be considered a starburst if its SFR is higher than the average of the host galaxy (Crowther et al., 2008).

It is suggested that radiation pressure, the pressure that photons exert on the surrounding gas and dust, might be enough to drive large scale galactic winds in starbursts (Andrews & Thompson, 2011). Evidence of radiation pressure can be seen as close as in our solar system, for instance the tail of passing comets always point away from the sun due to the pressure from solar photons. In a starburst, the pressure from the vast number of individual stars might add together, creating large scale winds.

2.3.3 Obscured Nuclei

In gas rich galaxies the nucleus, the most central few hundred parsecs, is surrounded by gas and dust. If the column density of the surrounding gas is high, it will obscure the most central regions from observations in the optical and infrared.

Since dust with temperatures around 100-150 K radiates strongly in the far infrared, assuming an approximate black body spectrum (Fig. 2.1), obscured galaxy nuclei are expected to emitt strongly at these wavelengths. In fact, the infrared radiation of the central regions often greatly exceeds the strength of the luminosity in the rest of the galaxy.

Still, it is likely that the most central parts of the nucleus are even warmer than what can be seen. Surrounding envelopes of ISM can absorb the escaping photons, effectively shielding the inside from our view. Aalto et al. (2015) give a possible model where the nucleus consists of a hot central core radiating in the mid-infrared, which in turn is surrounded by the cooler envelope that we see in the far infrared.

2.3.4 (Ultra-)Luminous Infrared Galaxies

Luminous infrared galaxies (LIRGs) are galaxies with an infrared luminosity between $L_{IR} = 10^{10} - 10^{11}$ L . Galaxies with even stronger IR-luminosity are instead known as Ultraluminous infrared galaxies (ULIRGs), their IR-luminosity exceeds 10^{12} L (Sanders & Mirabel, 1996). Common for this type of galaxies is that they are gas rich. It is believed that most of the (U)LIRGs are powered by AGNs, Starburst or even both, but since many contain obscured nuclei it is difficult to distinguish what powers them.

Common for most (U)LIRGs in the local universe is that they are mergers between two spirals (Elbaz & Cesarsky, 2003). As the galaxies merge, instabilities occur in the discs allowing gas and dust to travel towards the inner regions where it gives rise to an AGN or starburst. It is believed that (U)LIRGs go through evolutionary stages where they begin with heavily obscured nuclei. Later the SMBH will disperse the surrounding gas and dust through fast outflows (Sect 2.3.5), in the end leaving an exposed nucleus behind. To complete the picture, more knowledge on SMBH and its interaction with the host galaxy is needed.

2.3.5 Galactic outflows and winds: Feedback

Winds and outflows consist of gas and dust that are set into motion by some sort of process other than just gravitational pull. Radiation pressure on dust, supernovae explosions or magnetic fields near accretion discs can work as engines driving

this motion, creating everything from slow winds to relativistic jets (Veilleux, Cecil & Bland-Hawthorn, 2005, and sources within). AGNs and starbursts are powerful enough to drive winds and outflows on galactic scales, which in turn will affect the surrounding gas and dust. It is common for starburst-driven winds to be mechanically driven by stellar winds and supernovae explosions (SN), where the SN dominate the process unless the starburst is very young (. 10^7 yrs) (Veilleux, Cecil & Bland-Hawthorn, 2005). In AGN, the accretion disc around the central SMBH will increase its luminosity and thus its radiation pressure as the SMBH grows. At a critical mass or luminosity the radiation pressure will exceed the strength of gravitation and parts of the surrounding medium will get pushed away. This happens at the so called Eddington luminosity and the mass being pushed away is called an outflow.

Outflows interact with the surrounding galaxy creating so called *feedback*. Feedback is often discussed as if it is being positive or negative. Positive feedback will lead to perturbations in the surrounding gas, inducing star formation, while negative feedback instead quenches the star formation and SMBH growth by blowing away the building material from the center.

To observe molecular outflows, it is common to use spectroscopy. OH, CO and HCN are all molecules that have been used for this purpose, and it is usually the shape of the spectral peaks that helps indicating if it is an outflow that has been observed.

2.4 Galactic property estimation

The following section introduces ways of estimating galactic properties based on simple assumptions and previous observations.

2.4.1 Calculation of rotational and vibrational temperatures

One way to describe the excitation temperature is by the relation $N_u = \frac{N}{Q(T)} g_u e^{E_u/kT_{ex}}$, where $N_u = \frac{4\pi}{hcA_{ul}} S_\nu$ is the population in the upper state, N the total population, E_u the energy of the upper state, g_u the statistical weight of the upper level and Q(T) is a partition function (Imanishi, Nakanishi & Izumi, 2016a). By taking the logarithm we get the linear relation:

$$\ln N_u = \ln \frac{N}{Q(T)} g_u + \frac{E_u}{kT_{\mathsf{ex}}}, \tag{2.12}$$

showing that the excitation temperature is inversely proportional to the slope of the diagram with $\ln N_u$ on its y-axis and E_u/k on its x-axis. Rotational-vibrational transitions gives the following:

$$T_{\mathsf{vib}} = \frac{(E_u - E_l)/k}{\frac{\ln N_u}{\ln N_l}} = \frac{E_{ul}/k}{\ln \frac{(S_\nu)_u}{(S_\nu)_l}} \tag{2.13}$$

If the integrated flux for a transition is to be used, the frequency also must be considered:

$$T_{\mathsf{vib}} = \frac{E_{ul}/k}{\ln \frac{S_u}{S_l}\frac{\nu_l^2}{\nu_u^2}}, \tag{2.14}$$

which is similar to the form presented in Appendix B in Aalto et al. (2015b). The difference is that Aalto et al. (2015b) approximate E_{ul} as just the upper state energy E_u. Here the emission is assumed to be optically thin, that is to have an optical depth of $\tau < 1$, and to be co-spatial.

2.4.2 Calculation of the dynamical mass and the dense gas mass

The dynamical mass is an estimate based on Newtonian mechanics that tells which mass that is needed for a body with a rotational velocity $\mathrm{v}_{\mathsf{rot}}$ to have a stable orbit at the radius r, assuming the rotating body has negligible mass and no other forces are present. The equation is

$$M_{\mathsf{dyn}} = \frac{r\mathrm{v}_{\mathsf{rot}}^2}{G}, \tag{2.15}$$

where G is the gravitational constant. Rewriting the equation in $\mathrm{km\,s^{-1}}$, pc and mass in solar masses, we get:

$$\frac{M_{\mathsf{dyn}}}{M} = 2.3 \times 10^2 \left(\frac{r}{\mathrm{pc}}\right)\left(\frac{\mathrm{v}_{\mathsf{rot}}}{\mathrm{km\,s^{-1}}}\right)^2. \tag{2.16}$$

In reality, v is not obtained directly but through either the linewidth Δv of a line or the distance between central velocities and terminal velocities in a position-velocity diagram. A position-velocity diagram is a diagram with positions along one axis, and velocities along the other. The choice of positional axis will for a galaxy greatly affect the shape of the diagram. E.g, if the positional axis is chosen as the major axis of the galaxy, we get information about the rotation. A position-velocity diagram can be seen in Fig. 4.1.

Another mass of interest is the dense gas mass. This mass is based on observed correlations between HCN line luminosities and gas masses:

$$M_{\mathsf{dense}} = \alpha_{\mathsf{conv}} L_{\mathsf{HCN(1\text{-}0)}}. \tag{2.17}$$

Note that the line luminosity here is given in units of $\mathrm{K\,km\,s^{-1}\,pc^2}$. First to suggest this mass were Gao & Solomon (2004b) who suggested that the conversion factor should be $\alpha_{\mathsf{conv}} = 10\ M_\odot/(\mathrm{K\,km\,s^{-1}\,pc^2})$ based on densities and properties of cores in the Milky way. A more conservative factor $\alpha = 1/3.2\ M_\odot/(\mathrm{K\,km\,s^{-1}\,pc^2})$ suggested more appropriate for ULIRGs (García-Burillo et al., 2012) instead gives

$$M_{\mathsf{dense}} = 3.1 \times L_{\mathsf{HCN(1\text{-}0)}}. \tag{2.18}$$

If any other line than the J=1-0 line is observed, the dense gas mass calculated will be an upper limit, assuming optically thick emission that is thermalized up to the observed line. This is a result of the line luminosity being independent on J and

rest frequency under these conditions (Solomon & Vanden Bout, 2005). It is also possible to include an assumed line ratio between the observed HCN line and the HCN J=1-0 line to adjust for the fact that the conversion factor is based on HCN J=1-0 observations.

2.5 Fisher's exact test

To test for a possible correlation one may perform what is known as Fisher's exact test. This is appropriate if the data of interest are given in counts rather than continuous measurements. The test also calculates an exact p-value instead of an approximation relying on limit calculations, which makes it preferable to other methods in the case of a small sample. In the test, independent stochastic variables (i.e variables that do not affect each others properties) are assumed as well as them being identically distributed. The term identically distributed means that each random variable has the same probability distribution.

The null hypothesis in a Fisher test is that there is no non-randomization, in other words that any observed difference is an effect of pure randomness.

	Category 3	Category 4
Category 1	a	b
Category 2	c	d

Table 2.2: A typical Fisher-matrix. The categories are chosen so that category 1 and 2 can not contain the same sources, the same is valid for categories 3 and 4.

If the results from a study is summarized in a table like Table 2.2, the probability of the distribution being randomized is hypergeometric. Hence the probability obtaining the observed distribution is

$$p = \frac{\binom{a+b}{a}\binom{c+d}{c}}{\binom{n}{a+c}}, \tag{2.19}$$

where n is the total number of observations.

A significance level α should be chosen prior to the observation/experiment, that is the highest allowed probability of falsely rejecting the null hypothesis. Normally this is chosen to be 0.05. If the null hypothesis is rejected, that is if $p(k) < \alpha$, the test indicates that the distribution observed seems to be non-random and that some sort of statistical bias exists.

For more information about mathematical statistics, please consult Rice (2006).

3
Method

In this section, both the methods used to estimate properties of UGC 5101 will be presented, as well as assumptions and equations used in the statistical analysis of the eventual correlation between the L(HCN-VIB)/L_{FIR} ratio and molecular outflows.

3.1 Vibrational HCN and outflow data

Available data of vibrational transitions of HCN have been collected from the literature. A search in the ALMA archive was performed but no unpublished public data on the HCN vibrational lines was found.

Outflow data has primarily been collected from Veilleux et al. (2013), where outflows are observed through OH 119 μm profiles. We have focused on the v_{50}(abs) velocities which are median velocities estimated from fitting of absorption profiles where 50% of the absorption takes place at velocities above v_{50}(abs). v_{84}(abs) velocities where also available, however the internal velocity difference between the sources where almost identical and therefore likely to result in similar statistics.

3.2 Sample

The galaxy sample used in this thesis was based on the sample in Veilleux et al. (2013) with the addition of IC860, Zw049.057, IRAS 20414-1651, NGC 1377 and NGC 7469 (Aalto et al., 2015b; Imanishi, Nakanishi & Izumi, 2016a). The full sample with redshifts and far infrared luminosities are presented in Table 3.1. The chosen sample of galaxies primarily consists of (U)LIRGs and recent mergers. The sample should therefore consist of galaxies with gas rich nuclei that are heated by an energetic central engine in the form of an AGN or a compact starburst.

3.3 Calculation of line luminosities

In this work we adopt the same formulation as equation (1) in Solomon & Vanden Bout (2005) for calculation of line luminosities:

$$L = 1.04 \times 10^{-3} S\Delta V \nu_{rest} (1+z)^{-1} D_L^{\,2}, \tag{3.1}$$

where $S\Delta V$ is the velocity integrated flux of the observed peak in Jy km s^{-1}, ν_{rest} is the rest frequency in GHz, z the redshift and D_L the luminosity distance in Mpc.

Table 3.1: Sample galaxies

Name	z	D_L (Mpc)	log L_{FIR} [L]
(1)	(2)	(3)	(4)
Arp 220W	0.018126	75.5	12.03
IC860	0.011164	50	11.17
I Zw 1	0.05890	248	11.46
Zw049.057	0.012999	56.4	11.27
Mrk 231	0.042170	181	12.31
Mrk 273	0.037780	162	12.08
NGC 1377	0.005977	23	10.13
NGC 4418	0.007268	34.9	11.00
NGC 7469	0.016317	62.7	11.40
UGC 5101	0.039367	168	11.87
08572+3915	0.05835	254	12.01
12112+0305 NE	0.073317	324	12.22
13120-5453	0.030761	133	12.18
13451+1232	0.12174	551	12.03
15250+3609	0.055155	238	11.92
17208-0014	0.042810	181	12.39
20414-1651	0.087084	378	12.06
20551-4250	0.042996	180	11.92
22491-1808	0.07776	334	12.09

Note: Col. (1): Galaxy name. Col. (2): Redshift. Col. (3): Luminosity distance retrieved from NED. Col. (4): Far infrared luminosity retrieved from Sanders et al. (2003) and Kim & Sanders (1998).

The luminosity is given in L . This equation corrects for redshift and has been used by several of the references (e.g Imanishi, Nakanishi & Izumi, 2016b,a; Martín et al., 2016), making it appropriate for comparison between the results. However another version of Eq.3.1, Eq.(3) in Solomon & Vanden Bout (2005), had to be used to get the luminosity for UGC 5101 in units required by Eq.(2.18):

$$L = 3.25 \times 10^7 S\Delta V \nu_{obs}^{-2} (1+z)^{-3} D_L^2. \tag{3.2}$$

The luminosity L is given in units of $\mathrm{K\,km\,s^{-1}\,pc^2}$, assuming the integrated intensity SΔ V is given in $\mathrm{K\,km\,s^{-1}}$, the frequency ν_{obs} is given in GHz and the luminosity distance D_L is given in Mpc.

3.4 UGC 5101

UGC 5101 is a LIRG with a redshift of $z = 0.039$ and a luminosity distance of D_L=186 Mpc. In Fig. 3.1, a red-brown band of obscuring material can be seen to

cover the otherwise luminous galaxy. This is a band of gas and dust that absorbs the starlight as it circles the galaxy. Together with the elongated shape of the galaxy, this band helps in interpreting that the galaxy is being viewed close to edge-on.

While observations and calibration of the UGC 5101 data is not part of this work, calculations and estimations of properties are presented here. The observational data used will be presented in a forthcoming paper (Hallqvist et al., in prep.).

Figure 3.1: Hubble space telescope image of UGC 5101. Credit: NASA, ESA, the Hubble Heritage (STScI/AURA)-ESA/Hubble Collaboration and A. Evans

3.4.1 The vibrational temperature

To estimate the vibrational temperature of UGC 5101, Eq.(2.14) was used with $E_{ul} \approx E_u$. Even though this is the simplified equation, it was a good enough approximation since the optical depth is unknown and presents a greater uncertainty. Since the emission is assumed to be optically thin the temperature was calculated for some different values of optical depths. This was done by multiplying the ground state flux with the optical depth (sect. 2.4.1).

3.4.2 The dynamical mass and dense gas mass

To calculate the dynamical mass, the rotational velocity was approximated from position velocity diagrams of HCN (see Sect. 4.1.2). v_{rot} was taken as half the distance between the initial and final velocity in the position-velocity diagram. Another way could have been to use the width of the spectral line at full width at half maximum. This method was abandoned because of absorption profiles at the line peaks, leading to trouble fitting a Gaussian curve without large uncertainties in the resulting values. The pv-diagram adopted velocities will be a bit wider than full width at half maximum values from the spectrum, possibly overestimating the velocity.

To get the dynamical mass Eq.(2.16) was used, with the ratio chosen to represent the area of the nuclear HCN emission. Since the emission can be approximated as

elliptically distributed in reality, the radius was chosen to give a circle with same area as the approximated ellipse.

The dense gas mass was calculated using Eq. (2.18). Since this equation is based on a relationship between the HCN J=1-0 line and dense gas masses, using the J=3-2 value gave an upper limit.

3.5 Statistical tests

To look for correlation between the L(HCN-VIB)/L_{FIR} ratio and outflows, Fisher's exact test (Sect. 2.5) was performed. This method was chosen since the available sample was small. Aalto et al. (2015b) who first suggested a possible correlation divided outflows into fast outflows (velocities greater than the nuclear escape velocity), slow outflows (velocities smaller than the escape velocity) and inflows (gas with velocities towards the nucleus). This use of categories rather than continuous values makes Fisher's exact test a good method.

Pairing weak outflows with inflows and by dividing the ratios into high or low, the observed sources were placed into a 2-by-2 Fisher-matrix (see Table 2.2). The probability of the distribution being random was then calculated using Eq.(2.19). We adopted a significance level of $\alpha = 0.05$ for rejection of the null hypothesis of no non-randomization.

4
Results

This section both present parts of new observations of the ULIRG UGC 5101 (Hallqvist et al., in prep.) as well as a continuation of the statistics first attempted in Aalto et al. (2015b). Additional observations from the literature, as well as the here presented observations from UGC 5101 are included.

4.1 UGC 5101

An HCN-VIB peak is detected in UGC 5101. Table 4.1 present the measured fluxes as well as the calculated luminosities and fitted source size. A summery of estimated properties for UGC 5101 are presented in Table 4.2 and the following sections will explain them further.

Table 4.1: Observed properties for UGC 5101

Line	Integrated intensity [Jy km s^{-1}]	L [10^3 M]	L' [10^7 K km s^{-1} pc^2]	Source size [pc × pc]
HCN J=3-2	26.6	199.8	30.8	651 × 220
HCN J=3-2 ν_2=1f	2.5	18.9	2.9	

Note: Source size is given as major × minor axis lengths of an elliptical Gauss fit of the emission.

4.1.1 The vibrational temperature

Using Eq. (2.14), the vibrational temperature for HCN-VIB is calculated to 442 K. Since the optical depth is unknown we calculate the temperature for three different optical depths to give an indication of how it is affected. If we assume an optical depth of $\tau = 5$, the ground state flux is multiplied with this factor resulting in a temperature of T_{vib}=264 K. With an optical depth of $\tau = 10$ the temperature then would result in T_{vib}=225 K, and an optical depth of $\tau = 20$ finally would give T_{vib}=196 K.

4.1.2 The rotational velocity

The rotational velocity of UGC 5101 is estimated from the HCN major axis pv-diagram in Fig.4.1. Estimating half the vertical width of the second contour in the

diagram, we get a mean rotational velocity of $v_{rot\text{-}HCN} = 400$ km s^{-1}. The galaxy is approximated as being viewed edge on (Sect. 3.4), for other angles the velocity should be multiplied by $\sin^{-1} i$, where i is the inclination.

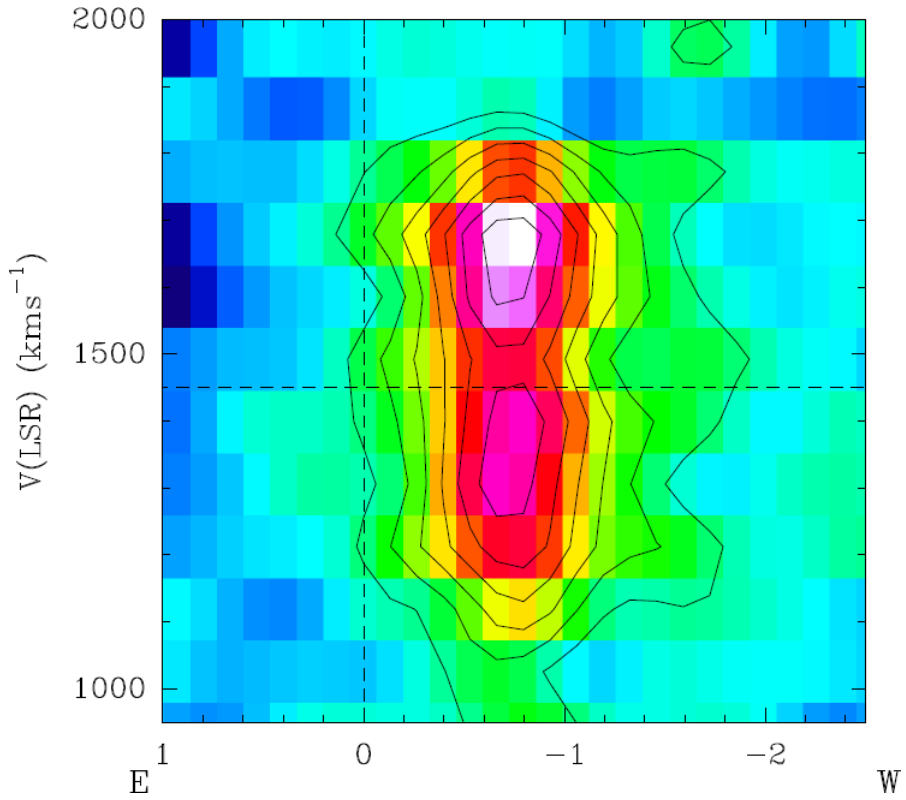

Figure 4.1: Position velocity diagram of HCN in UGC 5101. The contours mark signals in steps of intensities of 3σ. The x axis gives the position in arcseconds while the y axis give the velocity in km s^{-1}. Figure from Hallqvist et al. (in prep.).

4.1.3 Dynamical and dense gas masses

Using Eqs. (2.16) and (2.18), both the dynamical mass and an upper limit of the dense gas mass are estimated. The flux values used are the integrated intensities within an average radius of 378 pc, with corresponding luminosities presented in Table 4.2. Here the radius of 378 pc was chosen to give the same area as the fitted ellipse (Tab.4.1). Within this radius $M_{dense}(H_2) = 9.5 \times 10^8 M$ while $M_{dyn} = 1.4 \times 10^{10} (\sin i)^{-2} M$.

Table 4.2: Estimated properties for UGC 5101

v_{rot}	400 km s^{-1}
M_{dyn}	$1.4 \times 10^{10} (\sin i)^{-2} M$
$M_{dense}(H_2)$	$9.5 \times 10^8 M$
T_{vib}	442 K

4.2 Vibrational HCN and outflows in (U)LIRG:s

Collected luminosities, the L(HCN-VIB)/L_{FIR} ratio, OH outflow velocities and strength ratings of molecular outflows are presented in Table 4.3. The HCN-VIB luminosities have been recalculated using Eq. (3.1) with distances obtained from the NASA/IPAC Extragalactic Database (NED) (see Table 3.1). This may in some cases result in a slightly different luminosity compared with the original reference due to differences in adopted distances. In the cases where the references give only HCN-VIB luminosity values, and not fluxes, the luminosity has not been recalculated. Observations with a signal strength of $< 3\sigma$, where σ is the root mean squared noise, are considered non-detections.

The OH velocities are the v_{50}(abs) velocities from Veilleux et al. (2013), meaning they are the median velocities of fitted absorption profiles. Adopting the same distinction between fast and slow outflows as in Aalto et al. (2015b), a Y symbolizes an outflow with velocities faster than the escape velocity of the galaxy's nuclear region, while y means a slower. The letter n is used whenever no outflows or an inflow is observed.

4.3 Statistical tests

To check for a correlation between strong outflows and a high L(HCN-VIB)/L_{FIR} ratio, Fishers exact test is performed. Dividing the galaxies into categories, depending on if their HCN-VIB/FIR ratio is below or above 1×10^{-8} and if there are detected fast outflows or not, we get a 2-by-2 matrix like in Table 2.2. The result of Fisher's exact test performed on different cases are presented in the sections below.

4.3.1 L(HCN-VIB)/L_{FIR} vs OH outflows

Considering only the 12 sources in Table 4.3 with given OH velocities, Eq.(2.19) gives a probability of $p = 0.0076$ for the distribution being random. The distribution of the sources are shown in Table 4.4. With the significance level of 0.05, the null hypothesis of no non-randomization is rejected.

Figs. 4.2 and 4.3 show the outflow velocities for OH plotted against the L(HCN-VIB)/L_{FIR} ratio. It is not appearing to be a linear correlation with the actual velocities of outflows/inflows with the ratio, however a tentative trend can be seen. The choice of velocity definition primarily changes the distribution of the LIRGs, while the ULIRGs are less affected.

4.3.2 L(HCN-VIB)/L_{FIR} vs outflows with additional CO data

Including outflow data from both detections in CO and H_2 there are available data for 17 sources (I Zw 1 and NGC 7469 are not included). Since one of the sources has precisely R=1×10^{-8}, the test is performed for both the case when 1×10^{-8} is considered low, and for when it is considered high.

Table 4.3: L(HCN-VIB) vs. L_{FIR}

Name	L(HCN-VIB)	$\frac{L(HCN-VIB)}{L_{FIR}}$	v_{50}	Mol. outfl.	Ref
	[10^3 L]	[10^{-8}]	[km s^{-1}]	Y/y/n	
(1)	(2)	(3)	(4)	(5)	(6)
J=3-2					
Arp 220W	63	4.91	21	y	[1]
IC860	2.75	1.86	-	n	[2]
I Zw 1	No det.	0	...		[4]
Zw049.057	5.93	3.19	-	y	[2]
Mrk 231	14	0.68	-237	Y	[3]
Mrk 273	<4	<0.3	-201	Y	[9]
NGC 4418	5.38	5.38	111	n	[2][5]
NGC 7469	No det.	0	-		[4]
UGC 5101	18.9	2.5	-9	y	[7]
08572+3915	No det.	0	-489	Y	[4]
12112+0305 NE	14	0.84	-117	Y	[4]
13451+1232	No det.	0	...	Y	[4]
15250+3609	No det.	0	189	n	[4]
20414-1651	No det.	0	-	y	[4]
20551-4250	2.16	0.26	-381	Y	[6]
22491-1808	14	1.14	99	n	[4]
J=4-3					
Arp 220W	145.21	13.55	21	y	[1][2]
NGC 1377	-	1	-	Y	[2]
NGC 4418	13.44	13.44	111	n	[2][5]
13120-5453	-	<0.2	-195	Y	[2][8]
17208-0014	93.12	3.79	51	Y	[2]
20551-4250	4.49	0.57	-381	Y	[6]

Note: Col. (1): Galaxy name. Col. (2): Line luminosity of the HCN-VIB line calculated according to eq. (3.1). Col. (3): Ratio between the HCN-VIB line luminosity and the far infrared luminosity. Col. (4): Median outflow velocities, v_{50}(abs), from fitted OH absorption profiles by Veilleux et al. (2013). Col. (5): Outflows with velocities greater than the nuclear escape velocity are noted with Y, outflows with smaller velocities with y, and inflows with n. Col. (6): References for the HCN-VIB observations: [1] Martín et al. (2016); [2] Aalto et al. (2015b); [3] Aalto et al. (2015a); [4] Imanishi, Nakanishi & Izumi (2016a); [5] Sakamoto et al. (2010); [6] Imanishi, Nakanishi & Izumi (2016b),[7] Hallqvist et al. (in prep.), [8] Privon et al. (2017), [9] Aladro (in prep.). References for the outflows/inflows in Col. 5: Arp220 (Sakamoto et al., 2009), IC860 (Aalto et al., 2015b), Zw049.047 (Falstad et al., 2015), IRAS 13451+1232 (Dasyra & Combes, 2011), IRAS 20414-1651 (Spoon et al., 2013), NGC 1377 (Aalto et al., 2016), IRAS 17208-0014 (García-Burillo et al., 2015). The primary reference for the unmentioned sources, as well as the sources with given velocities in Col.4 are Veilleux et al. (2013).

	R6 1×10^{-8}	R>1×10^{-8}
Fast outflow	6	0
Slow outflow or inflow	1	5

Table 4.4: Fisher-matrix for the 12 sources with known OH velocities.

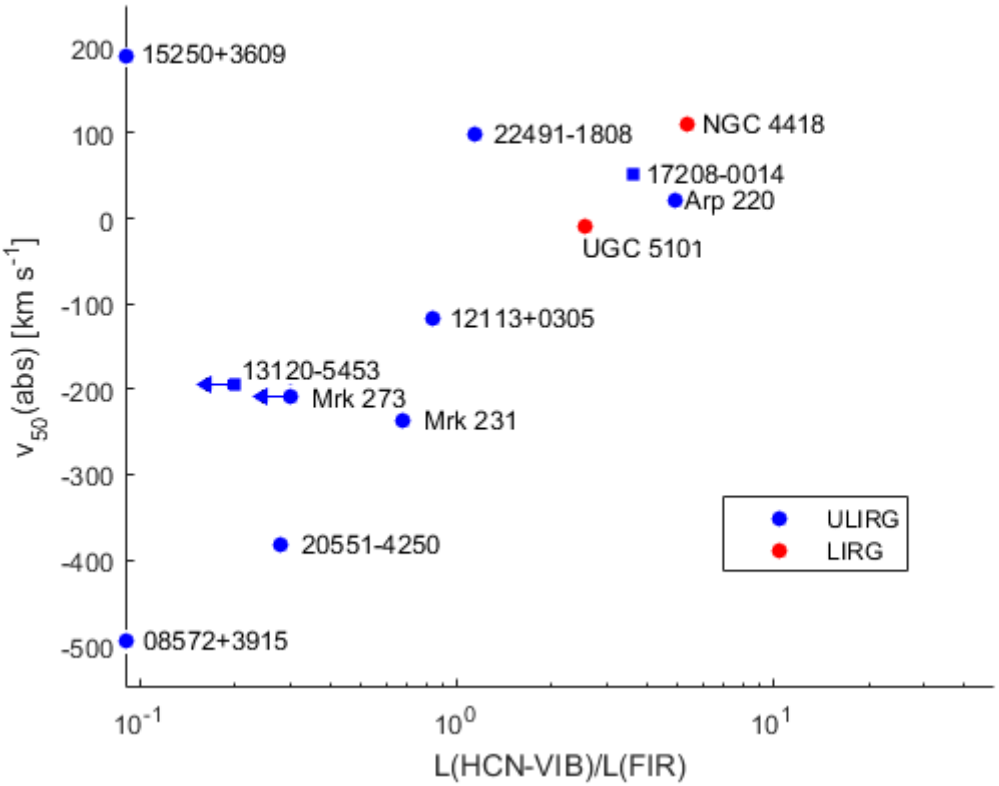

Figure 4.2: Scatter plot with L(HCN-VIB)/L_{FIR} on the x-axis and OH v_{50}(abs) velocities from Veilleux et al. (2013) on the y-axis. Sources with both HCN J=3-2 and J=4-3 detections have only been counted once and is marked by circles or squares respectively, upper limits are shown as arrows. Galaxies classified as ULIRGS are given blue markers while LIRGs are given red.

4.3.2.1 R=1×10^{-8} considered a high ratio

The distribution of the sources are presented in Table 4.5 resulting in a probability of $p = 0.041$ for the distribution being random. This is less than the chosen level of significance and the null hypothesis of no non-randomization can hence be rejected.

	R<1×10^{-8}	R> 1×10^{-8}
Fast outflow	7	2
Slow outflow or inflow	2	6

Table 4.5: Fisher-matrix for 17 sources with OH , CO and H_2 outflow data included. R=1×10^{-8} is considered a strong ratio.

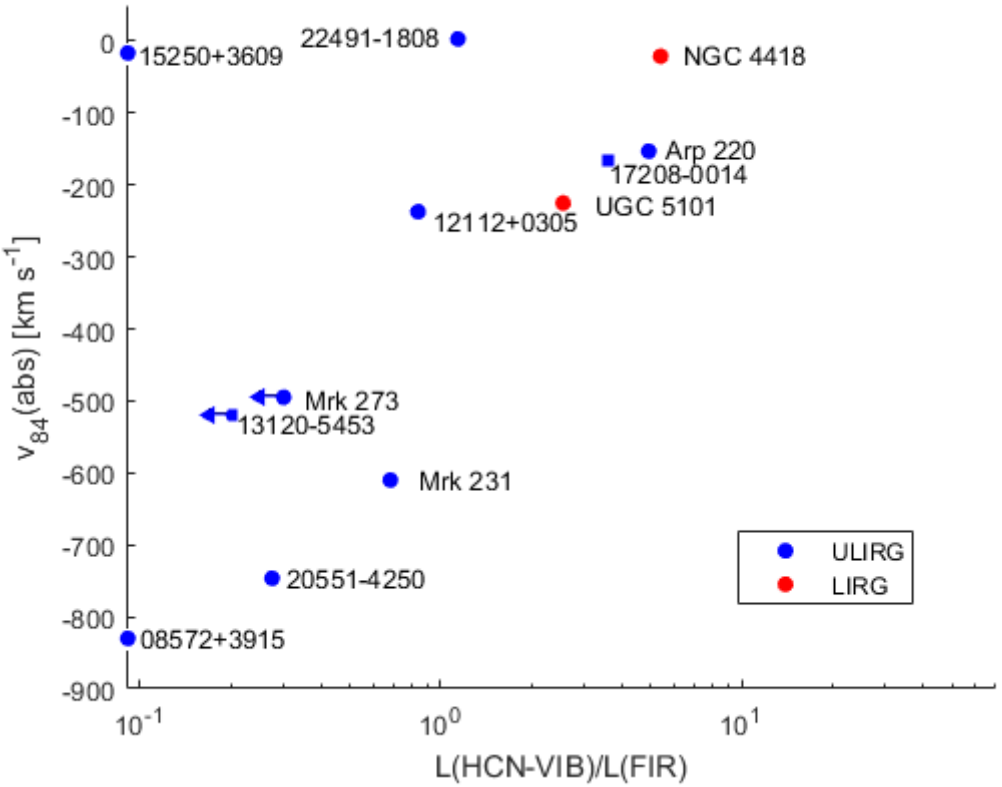

Figure 4.3: Scatter plot with L(HCN-VIB)/L_{FIR} on the x-axis and OH v_{84}(abs) velocities from Veilleux et al. (2013) on the y-axis. Sources with both HCN J=3-2 and J=4-3 detections have only been counted once and is marked by circles or squares respectively, upper limits are shown as arrows. Galaxies classified as ULIRGS are given blue markers while LIRGs are given red.

4.3.2.2 R=1×10^{-8} considered a low ratio

The distribution of the sources are presented in Table 4.6, resulting in a probability of the distribution being random of $p = 0.013$. This is less than the chosen level of significance and the null hypothesis of no non-randomization is rejected.

	R≤1×10^{-8}	R>1×10^{-8}
Fast outflow	8	1
Slow outflow or inflow	2	6

Table 4.6: Fisher-matrix for 17 sources with OH , CO and H_2 outflow data included. R=1×10^{-8} is considered a weak ratio.

5
Discussion

In this section we will discuss possible interpretations of the results as well as limitations of the data used, problems with the statistical test and other caveats.

5.1 UGC 5101

The calculated vibrational temperature is likely to be underestimated due to the assumption that HCN-VIB and the ground state HCN is co-spatial. Since HCN-VIB reside in a more central, and thus smaller region, the $(v = 1)/(v = 0)$ ratio will be lower than what it is in reality. However we get the opposite result when we include optical depths in the calculations, indicating that the temperature is overestimated when we assume optically thin lines. With the firm lower limit of $T_{vib} = 100$ K below which HCN-VIB will not be excited, we hence get a wide range of possible temperatures. Comparing with other sources we find a similar observed vibrational temperature in Mrk 231 (Aalto et al., 2015a) with a difference of 50 K, UGC 5101 having the higher value. For galaxies with compact obscured nuclei the temperature would instead be much higher, e.g Arp 220 which would get an uncorrected temperature of $T_{vib} = 735$ K, using Eq. (2.14) on values from Martín et al. (2016).

From the simple estimations of the dense gas mass and dynamical mass of UGC 5101, it can be see that $M_{dense}/M_{dyn} = 0.068$ within a radius of $r = 378$ pc, where r was chosen to represent the same area as the fitted ellipse of HCN emission (see Tab. 4.1). This means that the dense gas only makes up a small part of the dynamical mass available in the nucleus. Here, line blending may lead to an incorrect estimation of the rotational velocity, but this will affect the luminosity estimation of the line as well. If the line width at full width at half maximum would have been used to estimate the velocity instead, it would have been lower.

Given that our calculated M_{dense} is an upper limit, it is of interest to compare it with the literature. Comparing with HCN J=1-0 data from (Imanishi, Nakanishi & Kohno, 2006), the dense gas mass would become $M_{dense} = 2.4 \times 10^8\ M_\odot$. This is around 25 % of our HCN J=3-2 based value, which means that the assumptions of an optically thick and thermalized medium is invalid. If we instead compare the HCN estimated dense gas mass in Sect.4.1.3 with the H_2 mass $M_{H_2} = 1.3 \times 10^9\ M_\odot$ estimated from CO by Wilson et al. (2008), it can be seen that the lower HCN-based result is an order of magnitude lower. However Wilson et al. (2008) base their values on a larger beam size, including a larger part of the galaxy in the mass calculations. The higher H_2 mass can also be a result of CO being able to trace colder and less

dense gas than HCN.

5.2 HCN-VIB and Outflows

The Fisher tests indicate that the high L(HCN-VIB)/L_{FIR} ratios are related to weak outflows as seen in v_{50}(abs). It is also reassuring that the distribution remains somewhat similar when v_{84}(abs) is used instead. However, the relation appears to be non-linear. For example, the sources with inflow velocities seem to scatter along the x-axis, while the outflow velocity could hint towards something more linear looking (Fig.4.2). This may indicate that the observed nuclei are less sensitive to inflowing gas than outflowing. As explained in Aalto et al. (2015b), the presence of warm and dense gas is a prerequisite for HCN-VIB to exist. A possible explanation is that the fast outflow reduces, e.g by removing the gas itself, the gas density or temperature, and thus the amount of HCN-VIB. An inflow does not have the same disturbing effect on the surrounding medium.

Highly obscured nuclei may be traced by absorption in the OH 65 μm line (OH65) (González-Alfonso et al., 2015). They have used a measure called the equivalent width, W_{eq}, which corresponds to the width of a rectangle with the height of the spectral peak that has the same area as the spectral line. Comparing the equivalent width of OH65 with outflow velocities, González-Alfonso et al. (2017) suggest that the fastest OH outflows arise in the most obscured sources. However, they point out that the reverse can not be seen. Our result, that a high L(HCN-VIB)/L_{FIR} ratio is related to slow outflows, also indicates that obscured sources don not have to have fast outflows. Since the sources with detected OH65 lines also are part of the sample from Veilleux et al. (2013), we can compare the L(HCN-VIB)/L_{FIR} ratios with W_{eq}(OH) (Fig. 5.1). The fact that the sources are almost completely distributed in a broad horizontal band indicate that the equivalent width of OH65 and the L(HCN-VIB)/L_{FIR} ratio trace different parts or physics of the galactic nuclei. González-Alfonso et al. (2015) mention that W_{eq}(OH65)>10 km s^{-1} indicate a core with T_{dust} > 60 K and N(H_{H_2})>10^{24} cm^{-2}. Given that a T_{dust} > 100 K is required to excite HCN to its vibrational state, HCN-VIB might trace a more central part of the galaxy nucleus or nuclei than OH65.

Both Aalto et al. (2015b) and González-Alfonso et al. (2017) suggest that the respective lines trace a rapid period of the AGN-Starburst evolution. Indeed, a high L(HCN-VIB)/L_{FIR} ratio may trace a period before the onset of strong feedback (Aalto et al., 2015b), while W_{eq}(OH65) remains broad before and after fast outflows have been launched. The timescale therefore seems to be longer for OH65.

Exploring the suggestion that HCN-VIB traces nuclei with black holes in an evolutionary state before the onset of strong feedback (Aalto et al., 2015b), it is worth taking a closer look at the properties of the galaxies in our sample. The largest L(HCN-VIB)/L_{FIR} ratios are found in the galaxies with the highest obscuration (e.g., Arp 220, NGC 4418, IRAS 17208-0014, IC860 and IRAS 22491-1808), which means that there is plenty of mass available to feed the SMBH. The lack of fast outflows, except in IRAS 17208-0014, indicate that the radiation or mechanical pressure from the accretion disc and starburst are too weak to expel the obscuring material. González-Alfonso et al. (2017) suggest that these sources (excluding IC 860

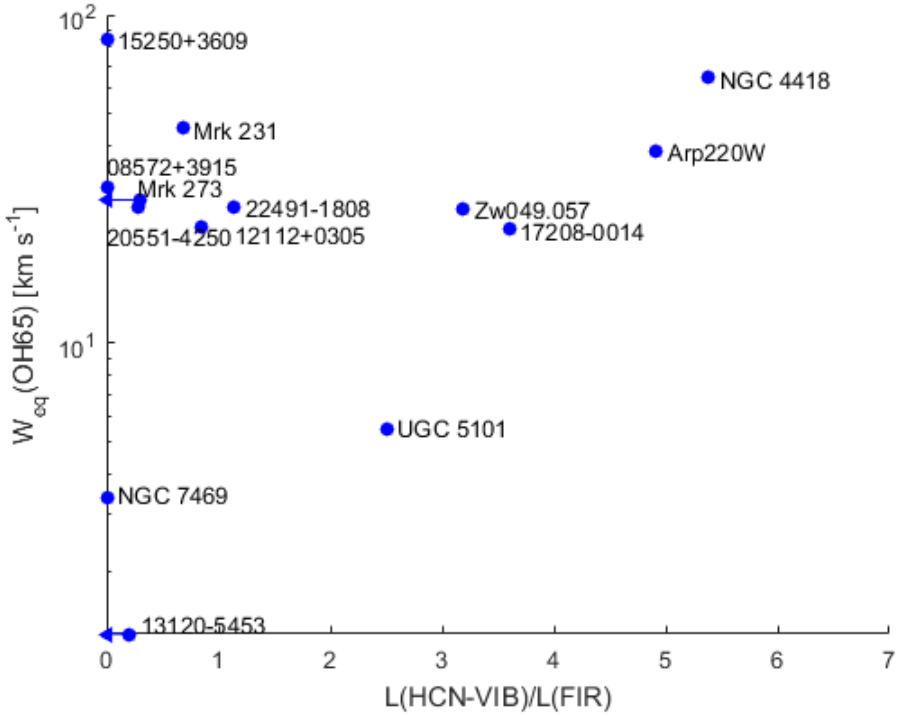

Figure 5.1: Scatter plot with L(HCN-VIB)/L_{FIR} on the x-axis and equivalent width W_{eq} from González-Alfonso et al. (2015) on the y-axis. Note the log-scale on the y-axis. Arrows indicate upper limits and sources placed on the y-axis are non-detections.

which is not part of their sample) have a larger solid angle of obscuring material, as large columns of gas will decrease the velocity of the outflows.

It is interesting to see that UGC 5101 is alone with W_{eq}(OH65)<10 in Fig. 5.1 and still has observed HCN-VIB. This strengthens the idea that OH65 and HCN-VIB trace different regions, otherwise there would be a discrepancy in the expected temperature for the region.

5.2.1 The contradicting sources

It was already pointed out in Aalto et al. (2015b), that IRAS 17208-0014 has a fast CO outflow (García-Burillo et al., 2015), which challenges the idea of a correlation between high L(HCN-VIB)/L_{FIR} ratios and slow outflows. Seen in OH absorption the image is reversed, the galaxy has an inflow that instead strengthens the idea of high L(HCN-VIB)/L_{FIR} ratios, indicating a lack of slow outflows. In our sample, IRAS 17208-0014 has the brightest far-infrared luminosity and contains a big gas reservoir of $6-7\times10^9$M (Downes & Solomon, 1998). The equivalent width is W_{eq}(OH65)>10 km s^{-1} (González-Alfonso et al., 2015), which is in line with the suggestion of González-Alfonso et al. (2017) that obscured nuclei accelerate outflows.

A possibility is that the outflow in IRAS 17208-0014 is recent and therefor still buried by columns of gas and dust. That way it can not yet be seen at shorter wavelengths since these are obscured by the surrounding medium. There is still enough

warm gas to excite HCN to its first vibrational state but the L(HCN-VIB)/L_{FIR} ratio will likely decrease as the outflow starts to expel the surrounding gas.

Another galaxy standing out from the other sources is IRAS 15250+3609. This galaxy is interpreted to have an outflow in HCO^+ rather than a HCN-VIB peak by Imanishi, Nakanishi & Izumi (2016a), but shows both a broad W_{eq}(OH65)(González-Alfonso et al., 2015) and absorption at 14 μm (Lahuis et al., 2007), together with a fast inflow. One possibility is that HCN-VIB is present, but that the peak is blended with the HCO^+ outflow profile. If we instead assume that it is a HCN-VIB peak that Imanishi, Nakanishi & Izumi (2016a) observed, Eq. (3.1) gives a L(HCN-VIB)/L_{FIR} ratio of 1.29. Going back to the comparison between L(HCN-VIB)/L_{FIR} ratios versus OH velocities the Fisher matrix 4.4 instead becomes Tab.5.1. Fig. 5.2 shows how the scatter plot would look assuming an HCN-VIB detection.

	R6 1×10^{-8}	R>1×10^{-8}
Fast outflow	6	0
Slow outflow or inflow	0	6

Table 5.1: Fisher-matrix for the 12 sources with known OH velocities, assuming 15250+3609 has a HCN-VIB detection.

The new probability is $p = 0.0011$, which is far less than the previous value of $p = 0.0076$, and hence an even stronger indication of a correlation. The same trend holds for the cases in Sect. 4.3.2.

5.3 Limitations on the data

The outflows from the sample of Veilleux et al. (2013) will not give the entire picture. It will not be possible to detect outflows or winds that appear behind the nuclei, these will be obscured by the nuclei themselves. The outflow velocities might also be underestimated due to projection, as is stated in Veilleux et al. (2013). Winds seen "edge-on" would in fact appear weaker than they are. This will, however, have little impact on the order of magnitude of the correlation.

Many of the observed sources suffer from wide line widths. This means that the lines may blend, thus making it difficult to distinguish between them. Since fluxes, luminosities and masses are all estimated from properties of the lines, the possible errors will spread throughout over- or underestimating the values depending on if the line eats or gets eaten by a nearby line. Using Eq. (3.1) an error in flux will propagate linearly, giving the same percentage error in luminosity. The same is valid using Eq. (2.18) for estimating the dense gas mass.

The observations of HCN-VIB are also limited by sensitivity. Imanishi, Nakanishi & Izumi (2016a) presented some sources with tentative detections, but since the signals had strength of $<3\sigma$ these detections were not included in our statistics. Even though an improved sensitivity might lead to these detections getting a better signal-to-noise ratio, including the sources would hardly affect the statistical outcome as the tests are constructed today. However they might have an impact on the possibility to see a linear relation purely in outflowing sources.

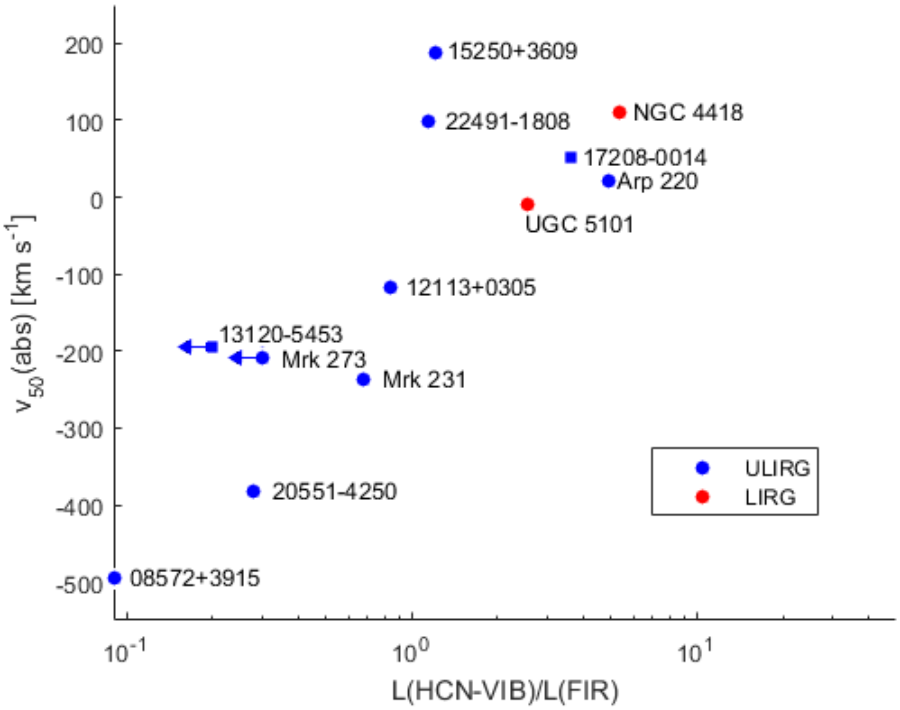

Figure 5.2: Scatter plot with L(HCN-VIB)/L_{FIR} on the x-axis and OH velocities from Veilleux et al. (2013) on the y-axis. Sources with both HCN J=3-2 and J=4-3 detections have only been counted once and is marked by circles or squares respectively, arrows represent upper limits. Galaxies classified as ULIRGS are given blue markers while LIRGs are given red.

5.4 The statistical analysis

One of the basic assumptions when using Fisher's exact test is that the studied variables of the galaxies will be identically distributed, i.e have identical probability distributions. If this actually is true requires some consideration. The random variables in our study are the L(HCN-VIB)/L_{FIR} ratio and the in-/outflow. Now, if the variables are to be identically distributed the probability for an outflow in a galaxy would be expected to follow the same distribution as all the others. Unfortunately we cannot say if this is true or false. What instead can be argued is that the sample has been chosen to contain similar galaxies, and that this should increase the likeliness of the probability distributions being "identical".

Even though a galaxy may have detections of both the HCN-VIB J=3-2 and J=4-3 transitions, only one can be used in the statistics. Otherwise it is comparable to double counting one source, since the two transitions ultimately are believed to represent the same type of physical environment. With the current choice of limit for a strong versus weak line, this decision will not affect the result of the test. If the limit is chosen to be greater or less than 1×10^{-8} will however push the result towards two different directions, since the ratio for NGC 1377 happens to be given as exactly 1×10^{-8} in Aalto et al. (2015b). Without information about the

luminosity, NGC 1377 has one of the ratios that have not been recalculated in this work. Worth noting is that the choice of 1×10^{-8} as the edge between high and low ratios is slightly flexible. The choice was made based on an apparent natural division between the order of magnitude of the ratios for the sources, where galaxies with fast OH outflows all had ratios less than 1×10^{-8}.

6
Conclusion and Outlook

In this work, the possibility of a correlation between a high L(HCN-VIB)/L_{FIR} ratio and slow molecular outflows or inflows in (U)LIRGs have been explored. The sample was based on a sample containing (U)LIRGs from Veilleux et al. (2013), and was later reduced to 19 sources based on attempted observations of vibrationally excited HCN. New observations of UGC 5101 were also included as a case study, but a more detailed presentation will be given in a forthcoming paper (Hallqvist et al., in prep.). For the galaxies in the sample, the L(HCN-VIB)/L_{FIR} ratio was compared to the v_{50}(abs) velocity. By dividing the sources into categories depending on if fast outflows were observed or not, and by the strength of the L(HCN-VIB)/L_{FIR} ratio, Fisher's exact test was performed. The primary results of this thesis are:

- HCN-VIB is detected in UGC 5101 with a line luminosity of 18.9×10^3 L . This gives a strong L(HCN-VIB)/L_{FIR} of 2.5. Without opacity corrections the estimated vibrational temperature becomes $T_{vib} = 442$ K and the dense gas mass is $M_{dense} = 9.5 \times 10^8$ M . The dynamical mass inside $r < 378$ pc is estimated to 5.6×10^{10} M .
- By performing Fisher's exact test we get a strong indication of a correlation between L(HCN-VIB)/L_{FIR} ratios higher than 10^{-8} and the lack of molecular outflows with velocities exceeding the nuclear escape velocity. The null hypothesis of no non-randomization was rejected for several interpretations of the input data, strengthening the interpretation of an observed correlation. The significance level was set at 5%.

Comparing with published studies we draw the secondary conclusions:

- There is no indication of correlation between the tracers W_{eq}(OH65) and L(HCN-VIB)/L_{FIR} even though they both are suggested to trace obscured nuclei. This suggests that they trace different regions of galaxy nuclei. The observation of HCN-VIB in UGC 5101 especially show a temperature discrepancy if the two tracers are expected to trace the same region.

Since the statistical analysis is based on a small sample, it is of interest to include more sources. To look for HCN-VIB in more of the sources in Veilleux et al. (2013) would be an easy way of adding data, since the OH outflow velocities are already observed. It would also be of interest to add reliable inclination data for the existing galaxies to see if the angle of the nucleus affects what we detect. Ideally masses of the SMBHs would be included to follow up on the idea of HCN-VIB tracing a period of rapid growth (Aalto et al., 2015b). However this requires observations at other wavelengths and further assumptions of relations between the galactic bulge and the SMBH mass.

References

Aalto S. et al., 2016, A precessing molecular jet signaling an obscured, growing supermassive black hole in NGC 1377?, A&A, 590, A73

Aalto S. et al., 2015a, High resolution observations of HCN and HCO^+ J = 3-2 in the disk and outflow of Mrk 231. Detection of vibrationally excited HCN in the warped nucleus, A&A, 574, A85

Aalto S. et al., 2015b, Probing highly obscured, self-absorbed galaxy nuclei with vibrationally excited HCN, A&A, 584, A42

Aladro R., in prep.,

Andrews B. H., Thompson T. A., 2011, Assessing Radiation Pressure as a Feedback Mechanism in Star-forming Galaxies, ApJ, 727, 97

Antonucci R., 1993, Unified models for active galactic nuclei and quasars, ARA&A, 31, 473

Beckmann V., Shrader C., 2013, Active galactic nuclei. John Wiley & Sons

Carroll T. J., Goldsmith P. F., 1981, Infrared pumping and rotational excitation of molecules in interstellar clouds, ApJ, 245, 891

Choudhuri A. R., 2010, Astrophysics for physicists. Cambridge university press

Dasyra K. M., Combes F., 2011, Turbulent and fast motions of H_2 gas in active galactic nuclei, A&A, 533, L10

Downes D., Solomon P. M., 1998, Rotating Nuclear Rings and Extreme Starbursts in Ultraluminous Galaxies, ApJ, 507, 615

Draine B. T., 2010, Physics of the interstellar and intergalactic medium. Princeton University Press

Elbaz D., Cesarsky C. J., 2003, A Fossil Record of Galaxy Encounters, Science, 300, 270

Falstad N. et al., 2015, Herschel spectroscopic observations of the compact obscured nucleus in Zw 049.057, A&A, 580, A52

Gao Y., Solomon P. M., 2004a, HCN Survey of Normal Spiral, Infrared-luminous, and Ultraluminous Galaxies, ApJS, 152, 63

Gao Y., Solomon P. M., 2004b, The Star Formation Rate and Dense Molecular Gas in Galaxies, ApJ, 606, 271

García-Burillo S. et al., 2015, High-resolution imaging of the molecular outflows in two mergers: IRAS 17208-0014 and NGC 1614, A&A, 580, A35

García-Burillo S., Usero A., Alonso-Herrero A., Graciá-Carpio J., Pereira-Santaella M., Colina L., Planesas P., Arribas S., 2012, Star-formation laws in luminous infrared galaxies. New observational constraints on models, A&A, 539, A8

González-Alfonso E. et al., 2017, Molecular Outflows in Local ULIRGs: Energetics from Multitransition OH Analysis, ApJ, 836, 11

González-Alfonso E. et al., 2015, High-lying OH Absorption, [C II] Deficits, and Extreme L $_{FIR}$/M $_{H2}$ Ratios in Galaxies, ApJ, 800, 69

Hallqvist F., König S., Aalto S., , in prep.,

Imanishi M., Nakanishi K., Izumi T., 2016a, ALMA HCN and HCO+ J =3-2 Observations of Optical Seyfert and Luminous Infrared Galaxies: Confirmation of Elevated HCN-to-HCO+ Flux Ratios in AGNs, AJ, 152, 218

Imanishi M., Nakanishi K., Izumi T., 2016b, ALMA Investigation of Vibrationally Excited HCN/HCO^+/HNC Emission Lines in the AGN-Hosting Ultraluminous Infrared Galaxy IRAS 20551-4250, ApJ, 825, 44

Imanishi M., Nakanishi K., Kohno K., 2006, Millimeter Interferometric Investigations of the Energy Sources of Three Ultraluminous Infrared Galaxies, UGC 5101, Markarian 273, and IRAS 17208-0014, Based on HCN-to-HCO^+ Ratios, AJ, 131, 2888

Kim D.-C., Sanders D. B., 1998, The IRAS 1 Jy Survey of Ultraluminous Infrared Galaxies. I. The Sample and Luminosity Function, ApJS, 119, 41

Lahuis F. et al., 2007, Infrared Molecular Starburst Fingerprints in Deeply Obscured (Ultra)Luminous Infrared Galaxy Nuclei, ApJ, 659, 296

Lee E. J., Murray N., Rahman M., 2012, Milky Way Star-forming Complexes and the Turbulent Motion of the Galaxy's Molecular Gas, ApJ, 752, 146

Martín S. et al., 2016, The unbearable opaqueness of Arp220, A&A, 590, A25

Privon G. C. et al., 2017, The Dense Molecular Gas and Nuclear Activity in the ULIRG IRAS 13120-5453, ApJ, 835, 213

Rice J., 2006, Mathematical statistics and data analysis. Nelson Education

Sakamoto K., Aalto S., Evans A. S., Wiedner M. C., Wilner D. J., 2010, Vibrationally Excited HCN in the Luminous Infrared Galaxy NGC 4418, ApJ, 725, L228

Sakamoto K. et al., 2009, P Cygni Profiles of Molecular Lines Toward Arp 220 Nuclei, ApJ, 700, L104

Sanders D. B., Mazzarella J. M., Kim D.-C., Surace J. A., Soifer B. T., 2003, The IRAS Revised Bright Galaxy Sample, AJ, 126, 1607

Sanders D. B., Mirabel I. F., 1996, Luminous Infrared Galaxies, ARA&A, 34, 749

Sindhu P. S., 2012, Elements of Molecular Spectroscopy. New Academic Science

Solomon P. M., Vanden Bout P. A., 2005, Molecular Gas at High Redshift, ARA&A, 43, 677

Spoon H. W. W. et al., 2013, Diagnostics of AGN-Driven Molecular Outflows in ULIRGs from Herschel-PACS Observations of OH at 119 μm, ApJ, 775, 127

Tran H. D., 2003, The Unified Model and Evolution of Active Galaxies: Implications from a Spectropolarimetric Study, ApJ, 583, 632

Urry C. M., Padovani P., 1995, Unified Schemes for Radio-Loud Active Galactic Nuclei, PASP, 107, 803

Veilleux S., Cecil G., Bland-Hawthorn J., 2005, Galactic Winds, ARA&A, 43, 769

Veilleux S. et al., 2013, Fast Molecular Outflows in Luminous Galaxy Mergers: Evidence for Quasar Feedback from Herschel, ApJ, 776, 27

Wilson C. D. et al., 2008, Luminous Infrared Galaxies with the Submillimeter Array. I. Survey Overview and the Central Gas to Dust Ratio, ApJS, 178, 189

Wilson T. L., Rohlfs K., Hüttemeister S., 2009, Tools of radio astronomy, Vol. 5. Springer

Ziurys L. M., Turner B. E., 1986, Detection of interstellar vibrationally excited HCN, ApJ, 300, L19